ELSEVIER

Contents lists available at ScienceDirect

Materials Science & Engineering A

journal homepage: www.elsevier.com/locate/msea





Effects of Zr addition on lattice strains and electronic structures of NbTaTiV high-entropy alloy

Chanho Lee ^{a,b}, Gian Song ^{c,**}, Michael C. Gao ^d, Lizhi Ouyang ^e, Ke An ^f, Saryu J. Fensin ^a, Peter K. Liaw ^{b,*}

- a Materials Science and Technology Division, Los Alamos National Laboratory, Los Alamos, NM, 87545, USA
- b Department of Materials Science and Engineering, The University of Tennessee, Knoxville, TN, 37996-2100, USA
- c Division of Advanced Materials Engineering and Institute for Rare Metals, Kongju National University, Cheonan, Chungnam, 330-717, Republic of Korea
- ^d National Energy Technology Laboratory, Albany, OR, 97321, USA
- e Department of Physics and Mathematics, Tennessee State University, Nashville, TN, 37209, USA
- f Neutron Scattering Division, Oak Ridge National Laboratory, Oak Ridge, TN, 37831, USA

ARTICLE INFO

Keywords: High-entropy alloy In-situ neutron diffraction Plasticity Ductility Deformation behaviors

ABSTRACT

The room-temperature (RT) deformation behavior for two single-phase body-centered-cubic (BCC) refractory high-entropy alloys (RHEAs), NbTaTiV and NbTaTiVZr, has been comprehensively investigated via *in-situ* neutron-diffraction experiments. Our work shows that the addition of Zr leads to the transition of mechanical response from ductile to brittle behavior. The results of lattice-strain evolutions obtained from *in-situ* neutron diffraction for the ductile NbTaTiV RHEA exhibit atypical plastic-deformation behavior, i.e., the reduced plastic-anisotropic deformation, leading to an even distribution of the applied stress amongst the grains with different orientations rather than forming stress concentrations in {200}-oriented grains during plastic-deformation. Density functional theory (DFT) analysis shows that NbTaTiVZr has a lower electron density at the Fermi level, larger lattice distortion, and stronger charge transfer, as compared to NbTaTiV, suggesting higher strength and lower ductility in NbTaTiVZr, which are consistent with the current experimental results.

1. Introduction

A new class of multicomponent metallic alloys, which consists of four or more principal refractory elements in near-equiatomic ratios, referred to as refractory high-entropy alloys (RHEAs), have attracted attention due to their extraordinary properties at elevated temperatures, such as high strength, excellent softening resistance, sluggish diffusion, and outstanding thermal stability [1–8]. For example, first-reported bodycentered-cubic (BCC)-structured RHEAs, NbMoTaW and NbMoTaVW, retained their high yield strengths at elevated temperatures (up to 1600 °C), which is superior to that of Ni-based superalloys. Thus, RHEAs are being considered as next-generation ultrahigh temperature materials [3]. However, most reported single-phase RHEAs, including aforementioned two alloys, exhibit limited room-temperature (RT) ductility, owing to their availability of fewer slip system in the BCC structure [3, 9–12]. Although new HEAs design strategies have recently been developed, such as dual-phase HEAs and transformation-induced plasticity

(TRIP) HEAS [13,14], to overcome the strength-ductility trade-off at RT, these suggested deformation mechanisms for ductility could not function at high temperatures due to their single-phase instability at elevated temperature. Hence, there are extensive efforts to develop the ductile single-phase RHEAs, which exhibit excellent phase stability at high temperatures, but they usually indicate the large plasticity only in compression [15,16]. In fact, the tensile ductility is more important in forming them into components for engineering applications but, only few RHEAs exhibit the tensile ductility [13]. Despite facing such significant challenges, there are few theoretical efforts to study the contrasting plastic-deformation behavior between brittle and ductile RHEAs [17,18]. Due to the lack of the in-depth experimental study on the origin of excellent compressive plasticity in RHEAs, it brings more difficulties to further design the new RHEAs with tensile ductility.

Recently, there have been substantial efforts to enhance the strength of single-phase RHEAs with unique solid-solution strengthening, which is mainly contributed by lattice distortions [19,20]. For example, the

E-mail addresses: gasong@kongju.ac.kr (G. Song), pliaw@utk.edu (P.K. Liaw).

 $^{^{\}ast}$ Corresponding author.

^{**} Corresponding author.

NbTaTiV and NbTaTiVZr RHEAs possess a single BCC solid-solution phase, and strength of both alloys are dominantly contributed by solid-solution strengthening, which is mainly attributed to the lattice distortion. The addition of the Zr element effectively promotes distorted lattices, leading to the enhancement of yield strength about ~ 300 MPa, as compared to the NbTaTiV RHEA [19]. However, it is worth nothing that the compressive plasticity in NbTaTiVZr is significantly decreased increasing the degree of lattice distortion. theoretically-determined average lattice distortion for the NbTaTiV RHEA is in an excellent agreement with all experimentally-measured values, whereas, the values of locally-measured lattice distortion in NbTaTiVZr, which are obtained from the high-angle annular dark-field scanning-transmission-electron-microscopy (HAADF-STEM) technique (0.161 Å) in the [110] direction, show lower values than theoreticallyand other experimentally-determined lattice distortion (0.184 Å) [19]. From the results of discordance of lattice distortion value in the [110] direction, one could conclude that the level of lattice distortion is not uniformly distributed among grains with different orientations. The anisotropies of distorted lattices, in turn, could attribute to load concentration in certain grains during plastic deformation, and thus, it could result in reduced plasticity, compared to NbTaTiV RHEA. The objective of this study is to verify the above hypothesis, including the investigations of the deformation compressively-ductile NbTaTiV and compares it with that of relatively-brittle NbTaTiVZr RHEA, using state-of-the-art in-situ neutron diffraction at RT. Our results indicate that the typical lattice-strain evolution in brittle BCC-structure alloys, such as substantial elastic and plastic anisotropy, was observed in the NbTaTiVZr during deformation. However, the ductile NbTaTiV RHEA exhibited reduced plastic anisotropy, leading to even sharing of the applied stresses among the differently-oriented grains rather than forming stress concentrations in particular-oriented grains during deformation. Therefore, it is found that homogenous load-transfer could give rise to outstanding compressive ductility in single-phase BCC RHEAs. These experimental observations are further supported, using the density functional theory (DFT) calculations.

2. Experimental

The RHEAs used in this study, NbTaTiV and NbTaTiVZr, which are composed of equimolar ratios, were fabricated, using vacuum arc melting of high-purity elements (99.99 weight-percent purity) under an argon atmosphere. The melting chamber was evacuated to 10^{-5} torr to reach the desired melting environment. The ingots were flipped and remelted more than 10 times to achieve a homogeneous elemental distribution. Subsequently, the melted alloys were cast into a cylindrical water-cooled Cu mold, using the drop-casting technique. The cast samples were 4 mm in diameter and 50 mm in length. The synthesized alloys were cut (with an 8 mm length of each specimen) and sealed in a quartz tube with vacuum. The homogenization heat-treatments were conducted at 1200 °C for 3 days (NbTaTiV) and 12 h (NbTaTiVZr), using a box furnace. The different duration times for heat treatment in both RHEAs are due to their different homogenization conditions [19]. The microstructures for these two RHEAs were characterized, using scanning-electron microscopy (SEM) with a back-scattered electron (BSE) detector (Zeiss Auriga 40). The grain orientation was obtained, employing the Electron-Backscatter Diffraction (EBSD).

The compressive *in-situ* neutron-diffraction (ND) measurements of NbTaTiV and NbTaTiVZr were conducted under compression at the VULCAN Engineering Diffractometer of the Spallation Neutron Source (SNS), Oak Ridge National Laboratory (ORNL), to investigate the elastic and plastic deformation behavior at RT [21,22]. The compression experiments on the homogenized NbTaTiV and NbTaTiVZr alloys with a diameter of 4 mm and a length of 8 mm were conducted to investigate the elastic and plastic deformation behavior at RT, using a mechanical testing system (MTS) load frame. The ND facility employs the

time-of-flight (TOF) arrangement, which allows for the measurement of a wide range of d-spacings without further adjustment of samples or detectors. The *in-situ* neutron facility at VULCAN is equipped with two detectors, which allow for the collection of diffraction patterns corresponding to the lattice planes that are parallel to the loading and transverse directions, respectively. A 3×3 mm² slit and 2 mm collimators were used to cover a large volume of samples. A constant load-control mode with a stepwise-loading sequence was utilized during the measurement of the diffraction patterns. The measurement time of the neutron-diffraction data was 20 min at each stress level. When the stress level reached the yield strength, the control mode was changed from load to displacement-control modes with an incremental step of 0.2 mm. After that, single-peak fitting by a VULCAN Data Reduction and Interactive Visualization software (VDRIVE) program was employed to analyse the collected data [23].

To further understand the deformation behavior, density functional theory calculations were performed, using the Vienna Ab initio Simulation Package (VASP) [24,25]. The input atomic structures of the disordered NbTaTiV and NbTaTiVZr BCC solid solutions were constructed, using special quasi-random structures (SQS) [26] through the Alloy Theoretic Automated Toolkit (ATAT) package [27,28]. The 64-atom BCC and 125-atom BCC SQS models are detailed elsewhere [29]. Projector Augmented-Wave (PAW) potentials [30] and the Perdew-Burke-Ernzerhof (PBE) [31] gradient approximation for the exchange-correlation functional were used. Brillouin-zone integrations were performed, using the Monkhorst–Pack k-point meshes [32]. A smearing parameter of 0.2 eV was chosen for the Methfessel–Paxton [33] technique. The plane-wave energy cut-off was held constant at 300 eV.

3. Results

Fig. 1(a and b) show the typical single solid-solution microstructures with equiaxed grains for the homogenized NbTaTiV and NbTaTiVZr RHEAs. These micrographs exhibit equiaxed grains with the grains size of 200-400 µm for NbTaTiV and 350-500 µm for NbTaTiVZr, respectively, indicating no significant change in microstructural features after the addition of Zr in the NbTaTiV. Both alloys were found to have a random texture, as shown by the inverse pole-figure maps with the various colours highlighting the orientation of the grains [Fig. 1(c and d)]. Fig. 1(e and f) show the ND patterns corresponding to deformed NbTaTiV and NbTaTiVZr RHEAs, which were obtained from diffracted neutrons with the lattice planes perpendicular to the loading direction, during compressive elastic and plastic deformations at RT. The diffraction peaks in both the undeformed (an applied stress of 0 MPa) RHEAs corresponded to a single BCC phase with lattice parameters of 3.232 Å in NbTaTiV and 3.306 Å in NbTaTiVZr, respectively. The single BCC phase was retained during elastic and plastic deformation up to plastic strains of 22.2% in NbTaTiV and 11.9% in NbTaTiVZr, implying excellent phase stability in both HEAs under a large plastic strain without the presence of stress-induced phase transformations, such as twinning. The general trends in diffraction patterns corresponding to mechanical loads were also observed for both RHEAs, indicating an increase in the peak width and the decrease in the peak intensity during deformation. However, principal diffraction peaks [(110) and (200) planes] shifted by different amounts as a function of applied stress between NbTaTiV and NbTa-TiVZr. This trend implies that both alloys show different deformation behavior, even though they possess the same microstructure and phase in ambient conditions. Note that the detailed information of phase identification, microstructural evolution, and mechanical properties for the as-cast condition as well as homogenized NbTaTiV and NbTaTiVZr can be found from the References 19 and 20.

To further investigate the deformation behavior of NbTaTiV and NbTaTiVZr in detail, the evolution of principal diffraction peaks was specifically analysed by examining the various diffraction patterns at different applied stresses and plastic strains during *in-situ* neutron-

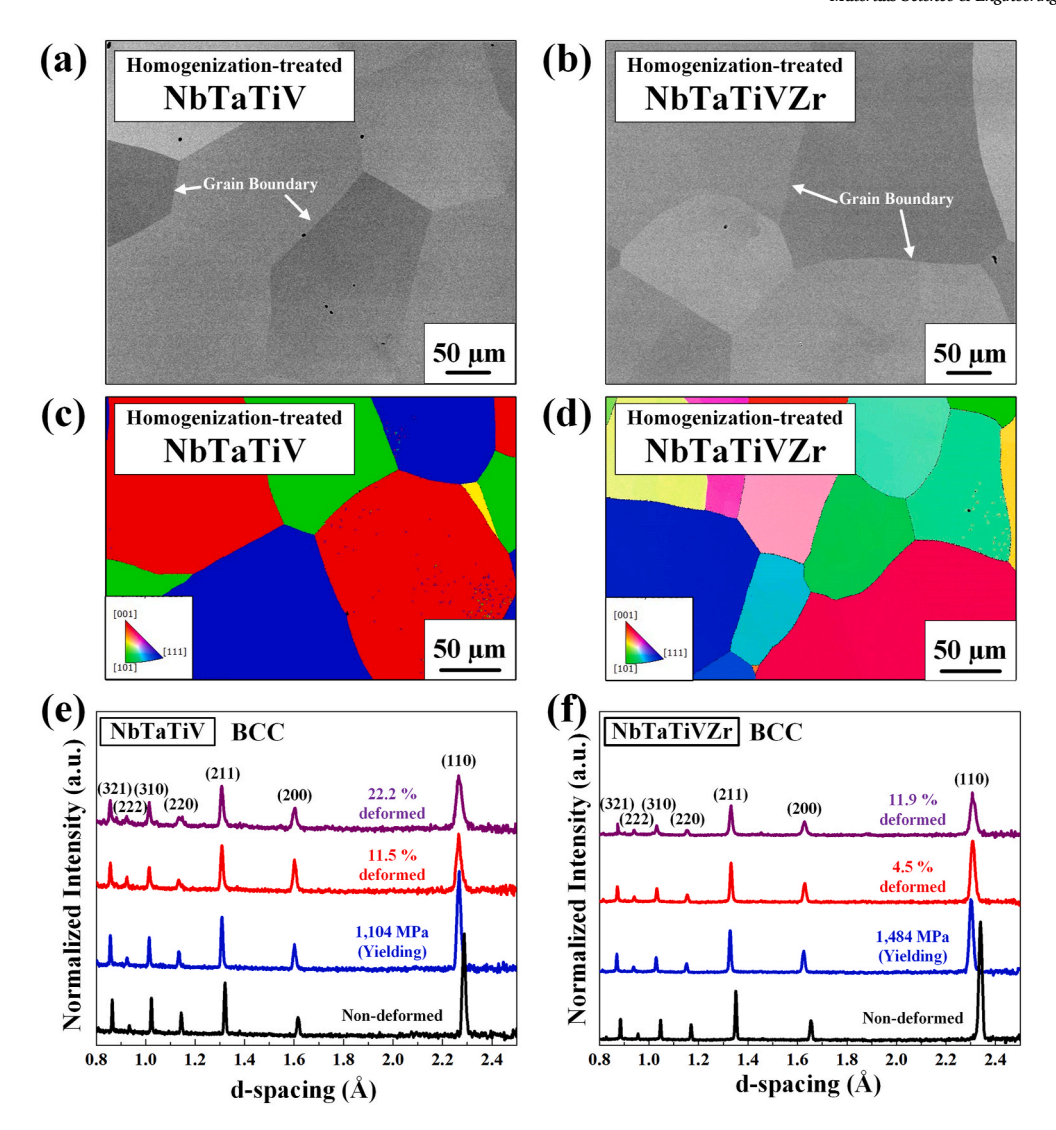


Fig. 1. (a), (b) SEM-BSE images of homogenization-treated NbTaTiV and NbTaTiVZr samples at 1200 °C for 3 days and 1200 °C for 12 h. (c), (d) EBSD with inverse-pole figure maps of homogenization-treated NbTaTiV and NbTaTiVZr samples. (e), (f) Neutron-diffraction (ND) patterns of NbTaTiV and NbTaTiVZr alloys during compressive elastic and plastic deformations at RT.

diffraction experiments, as shown in Fig. 2(a and b). The diffraction peaks corresponding to the (110) and (200) planes gradually shifted to smaller d-spacing for both alloys. The quantitative value of the d-spacing

change for NbTaTiV from the undeformed state to the plastic strain of 11.5% is 0.945% for (110) and 0.873% for (200), respectively. These

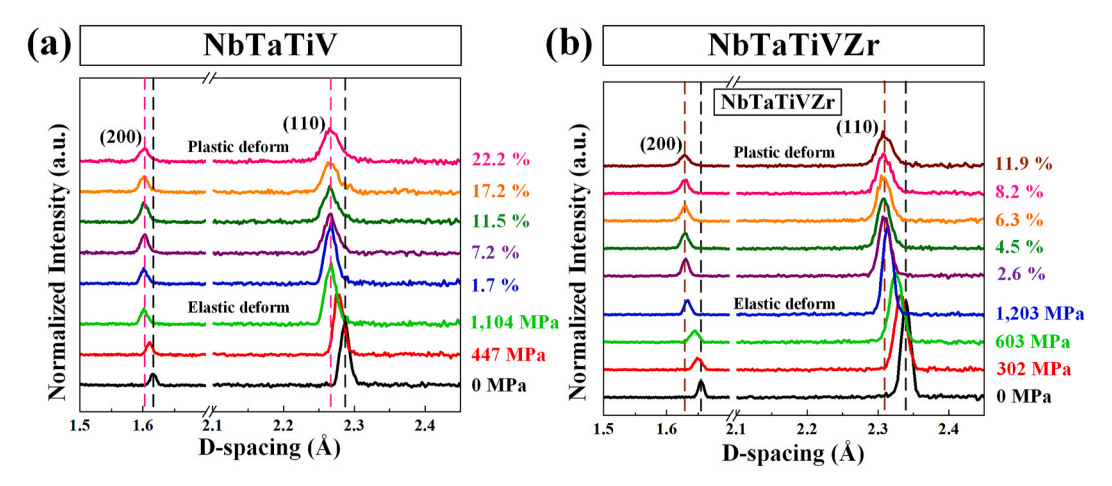


Fig. 2. (a), (b) The evolutions of principal neutron-diffraction peaks [(110) and (200) planes] of homogenization-treated NbTaTiV and NbTaTiVZr RHEAs, examining the various diffraction patterns at different applied stresses and plastic strains during *in-situ* neutron experiments.

values were estimated, using the relationship of $\frac{d_{hkl}^{11.5}-d_{hkl}^0}{dU} \times 100$, where $d_{hkl}^{11.5}$ is the d-spacing of hkl after a plastic strain of 11.5%, and d_{hkl}^{0} is the d-spacing in the undeformed state. In the case of the NbTaTiVZr [Fig. 2] (b)], the peak positions for (110) and (200) planes from the undeformed state to a plastic strain of 11.9% changed by 1.304% for (110) and 1.604% for (200), respectively, indicating larger variations in the peak positions, as compared to NbTaTiV at similar plastic strains. Note that the neutron-diffraction patterns for the NbTaTiVZr were measured until a maximum plastic strain of 11.9% due to the low compressive ductility (fracture at a plastic strain of $\sim 13.5\%$). On the other hand, NbTaTiV showed nearly same deviation of diffraction-peak shifting between (110) and (200) planes, exhibiting an orientation-independent diffraction peaks evolution. In general, the variations in the positions of diffraction peaks in single-phase metallic alloys is mainly due to lattice strains from deformation and are strongly dependent on grain orientations. However, the NbTaTiV shows orientation-independent diffraction peaks evolution during deformation at various applied stresses and plastic strains.

Based on the difference in the change of peak positions between NbTaTiV and NbTaTiVZr during elastic and plastic deformations in Fig. 2, the evolution of lattice strains in both alloys was analysed to clearly demonstrate the detailed deformation behavior and its direct correlation with mechanical properties, as presented in Fig. 3. Fig. 3(a and b) exhibit the engineering stress-strain curves [Fig. 3(a)] and corresponding lattice-strain evolutions [Fig. 3(b)], which were obtained from compressive in-situ neutron measurements of the homogenized NbTaTiV and NbTaTiVZr at a strain rate of $1\times 10^{-4}\,\mathrm{s^{-1}}$. The measured yield strength (σ_y) for NbTaTiV is about 1064 MPa, and there is no occurrence of fracture at a compressive strain of \sim 30%. In contrast, a significant increase in the yield strength by 350 MPa with considerable reduction in plasticity is observed after the addition of Zr into NbTaTiV. The improved yield strength of NbTaTiVZr is mainly due to the

substantial enhancement of solid-solution strengthening effects, which can also be attributed to severe lattice distortion [34]. Furthermore, these differences in the yield strengths and strains to failure between NbTaTiV and NbTaTiVZr can be attributed to distinct trends in the lattice-strain evolution [Fig. 3(b)]. The lattice strains was determined by the following equation:

$$\varepsilon_{hkl} = \frac{d_{hkl} - d_{hkl}^i}{d_{hkl}^i} \tag{1}$$

where d_{hkl} is the hkl d-spacing at the corresponding applied stress, and d_{hkl}^i is the hkl d-spacing of the undeformed state. At all applied stresses, NbTaTiVZr has larger amounts of lattice strains than NbTaTiV, resulting in smaller elastic modulus with lower elastic stiffnesses. Moreover, the deviation of lattice strains in four major grain orientations noticeably increased when the applied stress was closer to the yield strength, indicating typical elastic-anisotropic-deformation behavior.

During elastic deformation all grain orientations in both NbTaTiV and NbTaTiVZr have similar lattice strains with minor decreases in the lattice strain from $\{200\}$ to $\{110\}$ orientation in NbTaTiVZr [Fig. 3(b)], which could be quantified as a change in the elastic modulus as a function of orientation. The quantitative values of diffraction elastic moduli, E_{hkl} , in different crystallographic planes for NbTaTiV and NbTaTiVZr RHEAs are listed in Table 1. The less distribution of the lattice strain at the yielding point in NbTaTiV, compared to NbTaTiVZr, indicates the orientation-independent yielding behavior.

The relationship between the lattice strain and applied stress in four major grain orientations [{110}, {200}, {211}, and {310}] in NbTa-TiVZr and NbTaTiV is linear at all lattice strains during elastic deformation. Although, there is a change in the slope at ~ 1000 MPa which corresponds to the yield stress for NbTaTiV. Past this stress, the lattice strain in NbTaTiV is nearly constant in all grains during plastic deformation, whereas the NbTaTiVZr reveals that the lattice strain in {200}

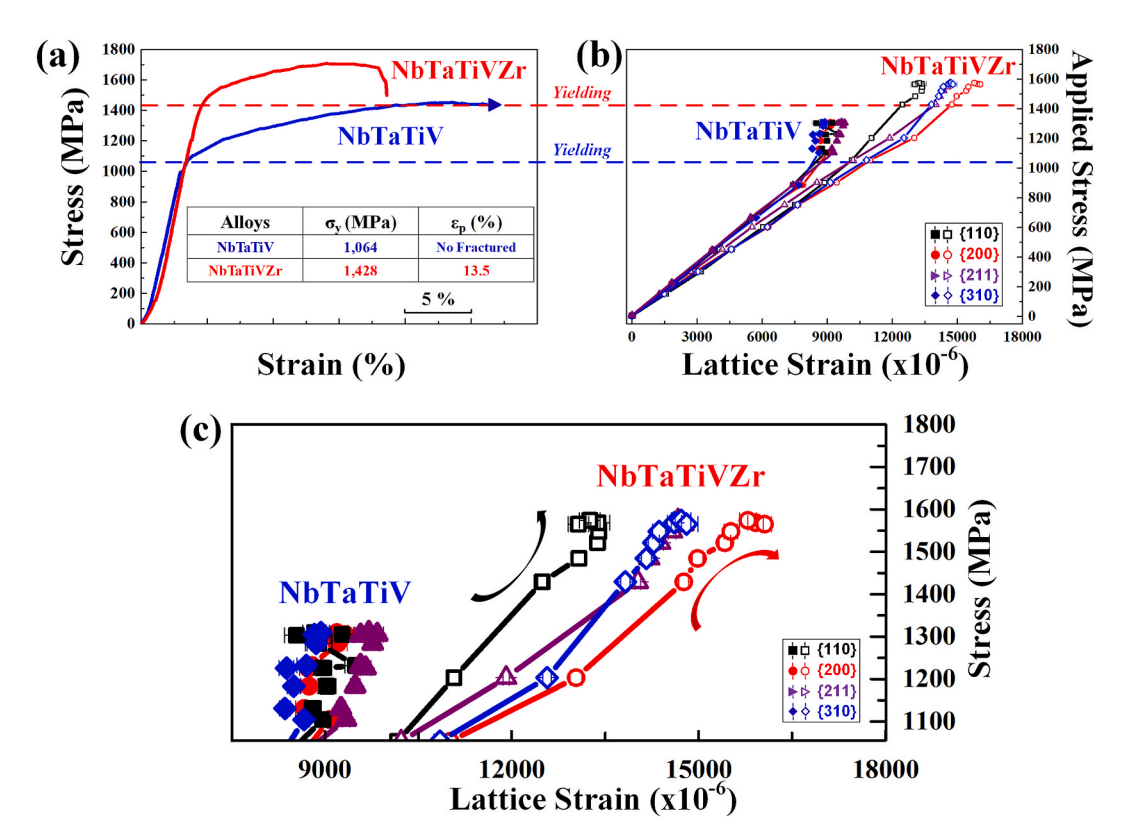


Fig. 3. (a) Compressive engineering stress-strain curves of NbTaTiV and NbTaTiVZr RHEAs recorded during *in-situ* compression experiments at RT with a strain rate of 1×10^{-4} s⁻¹. (b) Lattice-strain evolutions in the NbTaTiV and NbTaTiVZr RHEAs as a function of applied stresses obtained along the axial directions during *in-situ* ND experiments at RT. (c) Magnified lattice-strain evolution for NbTaTiV and NbTaTiVZr during only plastic deformations.

Table 1 The diffraction elastic moduli, E_{hkl} , of different crystallographic planes, {110}, {200}, {211}, and {310}, for the homogenized NbTaTiV and NbTaTiVZr RHEAs at RT.

Alloys	Parameters			
	Diffraction Elastic Modulus, E_{hkl} (GPa)			
Planes	{110}	{200}	{211}	{310}
NbTaTiV	122.5	115.9	121.7	117.9
NbTaTiVZr	106.7	93.0	101.3	96.4

grains significantly decline when the applied stresses exceeded 1520 MPa. At the same time, the lattice strain in $\{110\}$ grains become steeper. This variation of lattice strain in NbTaTiVZr can be indicative of the load transfer from $\{110\}$ to $\{200\}$ grains [35] and of anisotropic deformation as a function of grain orientation. An interesting point here is that the lattice strain versus applied stress relationship is similar for all orientations in NbTaTiV but the addition of Zr changes the plastic-deformation behavior.

Generally, the evolution in the lattice strain as a function of applied stress is dependent on orientation during elastic deformation owing to varying atomic-bond strengths and stiffnesses [35–37]. orientation-dependent elastic deformation leads to different slopes in the plot of the lattice strain as a function of the applied stress, indicative of varying diffraction elastic moduli. In case of conventional single BCC-phase metallic materials, the {200}-oriented grains have a lower elastic stiffness, whereas the {110}-oriented grains exhibit a higher elastic stiffness, compared to other orientations. Due to these intrinsic elastic characteristics of BCC alloys, the {200} and {110} grains show smaller and larger slopes in the plot of lattice-strain evolution with significant deviation of diffraction elastic modulus [35,38]. Following elastic deformation, the onset of yielding in grains occurs at varying applied stresses as a function of orientation. This feature can be postulated as strongly associated with the varying Schmid factors in these grains. In general, the {110} grains in BCC alloys tend to yield at an early stage, since the {110} orientation belongs to the slip system [38]. After the grain-to-grain yielding sequence, the slope of the {110} grain in the lattice-strain versus applied stress increases during plastic deformation, whereas the slope of the neighbouring grains [{200}-oriented grain] reduces due to the intergranular load transfer from yielding grains, indicating the anisotropic plastic deformation [35,36,39].

According to the fundamental understanding of the lattice-strain evolution in less ductile BCC alloys during elastic and plastic deformation, it is found that NbTaTiVZr shows typical deformation behavior with elastic and plastic anisotropy, as presented in Fig. 3(b). Especially, the apparent load transfer from {110} to {200}-oriented grains was clearly observed after a certain amount of plastic strains, which is due to the availability of fewer slip systems in brittle BCC alloys. Fig. 3(c) shows the magnified lattice-strain evolution for NbTaTiV and NbTa-TiVZr during only plastic deformations. While the values of latticestrains in all grains for NbTaTiV are almost constant (approximately 0.009) in whole plastic deformations, the values of lattice-strains in {110} and {200}-oriented grains in the relatively-brittle NbTaTiVZr significantly changed as a function of applied stresses. After the onset of yielding, the values of lattice-strains in both {110} and {200}-oriented grains are continuously increased from 0.1246 to 0.1337 for {110} grains and from 0.1474 to 0.1550 for {200} grains (when the samples were subjected to the plastic deformations of $\sim 11\%$). The opposite features of lattice-strain evolution between {110} and {200}-oriented grains over the plastic deformation of 11% apparently indicate the load transfer from {110} to {200}-oriented grains. The values of latticestrains for {110} grains decreased from 0.1337 to 0.1304, whereas its value in {200} grains continuously increased up to 0.1604 during a large plastic deformation of 18%. This uneven load partitioning could lead to stress concentrations in grains with specific orientations [{200}] grains in the present case] after a large amount of plastic deformation. In

contrast, NbTaTiV has nearly-elastic isotropic deformation as well as no orientation-dependent yielding behavior. Furthermore, there is significant load transfer from slip planes to neighbouring planes during plastic deformation. The distinction in the plastic deformation between the relatively brittle NbTaTiVZr and ductile NbTaTiV is clearly shown from the lattice-strain evolution as a function of micro-strain in {110} and {200} grains, as illustrated in Fig. 4. After elastic deformation with small amounts of micro-strains, NbTaTiVZr shows an orientation-dependent yielding, exhibiting a lower yield stress in {110} grains at lower lattice strains, as compared to {200} grains. Once, the alloy begins to plastically deform, the lattice strain in the {110} grains gradually decreases due to enhanced slip, whereas the lattice strain in the {200}oriented grains steadily increases. The deviation of lattice strains between {110} and {200} grains become larger after a plastic deformation of $\sim 10\%$, which could lead to the load concentration on {200} grains. The considerable stress (or load) concentration in a limited grain group is not in favour of ductility and may lead to fracture due to the development of local-stress concentration. However, NbTaTiV shows reduced plastic anisotropy, which is supported by the same lattice strains in {110} and {200} grains as a function of micro-strain, as presented in Fig. 4. This even load sharing could result in the reduction of the chance of single point failure. Consequently, these reduced plastic-anisotropicdeformation in the NbTaTiV RHEA accounts for the excellent compressive ductility due to the homogenous load-transfer between differently oriented grains.

4. Discussion

The mechanical properties of metallic materials are often strongly associated with the electronic structure, including the charge density and density of states (DOS). To further understand the effect of Zr alloying on the mechanical properties of the NbTaTiV HEA, the deformation charge density, density of states, and charge transfer with local deformation were studied by the density functional theory (DFT) analysis Fig. 5 compares the charge density difference (which is calculated by subtracting the superposition of atomic charge densities from the selfconsistent valence charge) and density of states in NbTaTiV and NbTa-TiVZr. Clearly, the electron-charge-difference distribution is more uniform in NbTaTiV than NbTaTiVZr, implying the addition of Zr induces fluctuations in delocalized free electrons. NbTaTiV has a higher DOS at the Fermi level than NbTaTiVZr. A higher DOS at the Fermi level is an indicator for greater ductility of metals. Fig. 6 correlates the charge transfer with local deformation. The local deformation is calculated from the principal axes of the average second moment of the

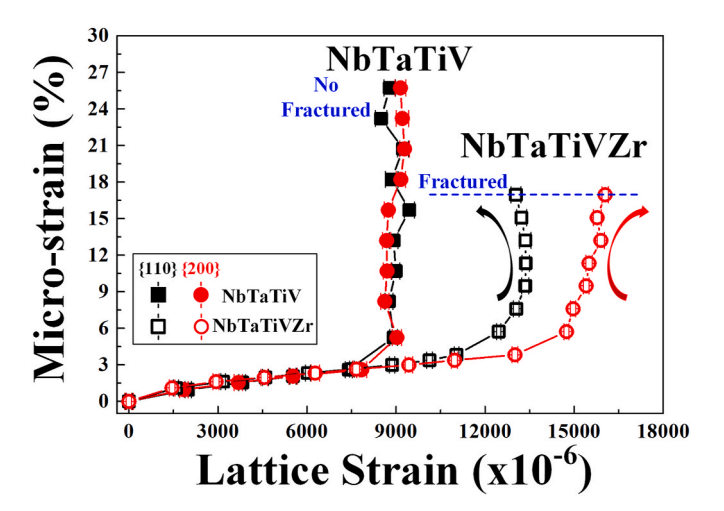


Fig. 4. Lattice-strain evolutions as a function of micro-strain for {110}- and {200}-oriented grains in the ductile NbTaTiV and relatively-brittle NbTaTiVZr RHEAs during *in-situ* ND experiments at RT.

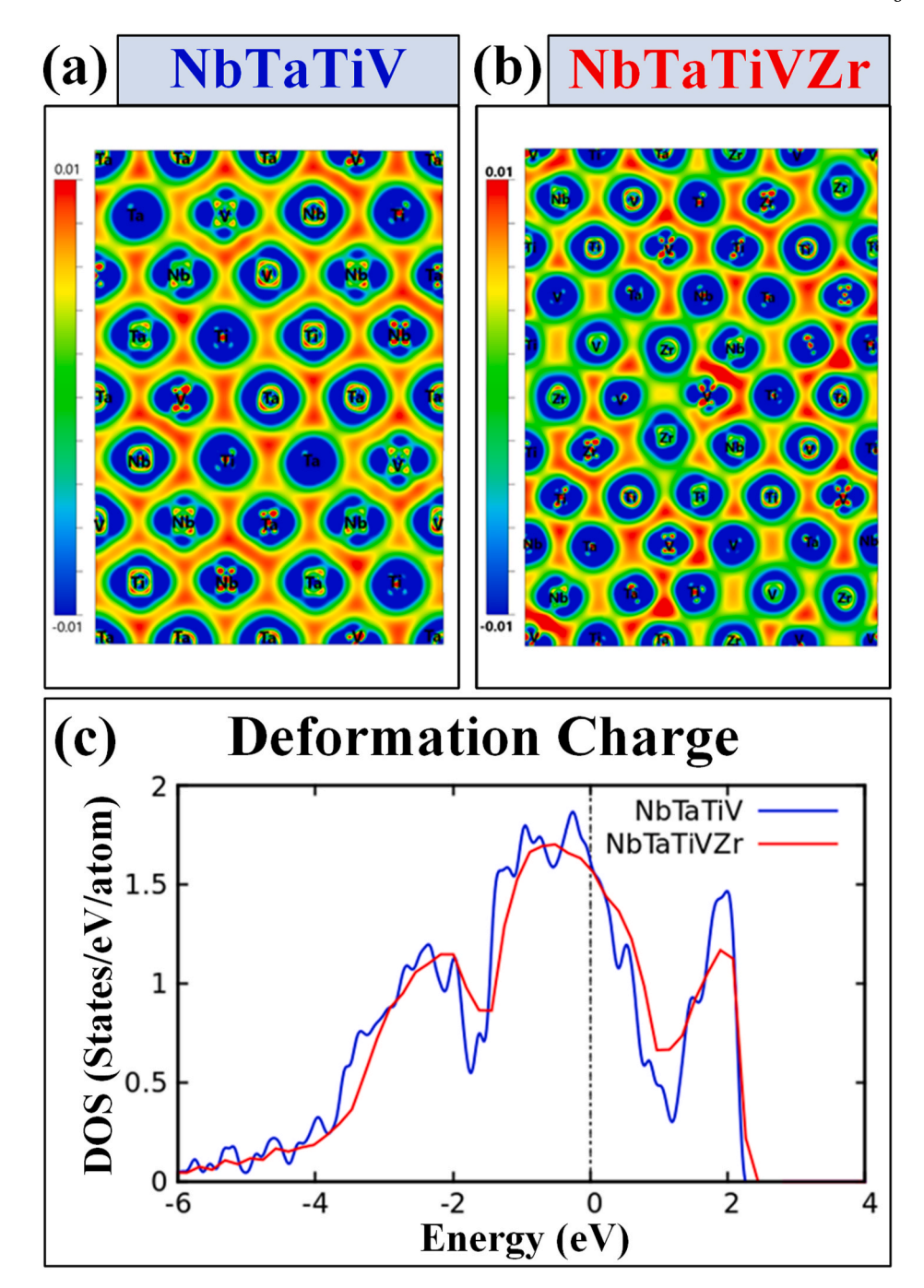


Fig. 5. The charge-density-difference plots for (a) NbTaTiV and (b) NbTaTiVZr. (c) The total electron density of states (DOS) of NbTaTiV and NbTaTiVZr. The vertical dashed line in (c) denotes the Fermi level.

displacements to the 8 nearest neighbours with respect to the principal axes of an ideal lattice with the same volume. The second moment, Δ_i , of the site, i, is computed as

$$\Delta_{i} = \sum_{j \in \{nearest \ neighbours \ of \ i\}} \left(\overrightarrow{r_{i}} - \overrightarrow{r_{j}}\right) \otimes \left(\overrightarrow{r_{i}} - \overrightarrow{r_{j}}\right)$$
(2)

Principal axes lengths are square roots of the eigenvalues of the second moment matrix Δ_i . The X axis is the average of the deformations of the principal axes. The elongation of the ellipse is propositional to the ratio of the longest principal axis and the shortest principal axis. Charge transfer is calculated, using the Bader charge analysis program [40]. Atom types are colour coded as labelled in the diagram. The values of average charge transfer are 0.2420, 0.4731, -0.7036, and -0.0137 for Nb, Ta, Ti, and V in NbTaTiV, and 0.3729, 0.6371, -0.6216, 0.1445, and

-0.5329 for Nb, Ta, Ti, V, and Zr in NbTaTiVZr RHEA, respectively. Overall, NbTaTiVZr shows larger fluctuation in both the electron charge transfer and local atomic deformation than NbTaTiV for Nb, Ta, Ti and V atoms, respectively. A large charge transfer implies stronger bond formation, i.e., Zr addition increases local deformation and promoted charge transfer, which leads to spread of charge and deformation distribution. A large local deformation indicates great lattice distortion. Combining the larger lattice distortion and stronger charge transfer in NbTaTiVZr explains its higher strength and lower ductility than NbTaTiV.

Previously, Lee et al. [34] have comprehensively investigated the strengthening mechanism for NbTaTiV and NbTaTiVZr RHEAs, using a theoretical model, first-principal calculations, and experimental verifications. As described in Fig. 1, the two present RHEAs possess a single

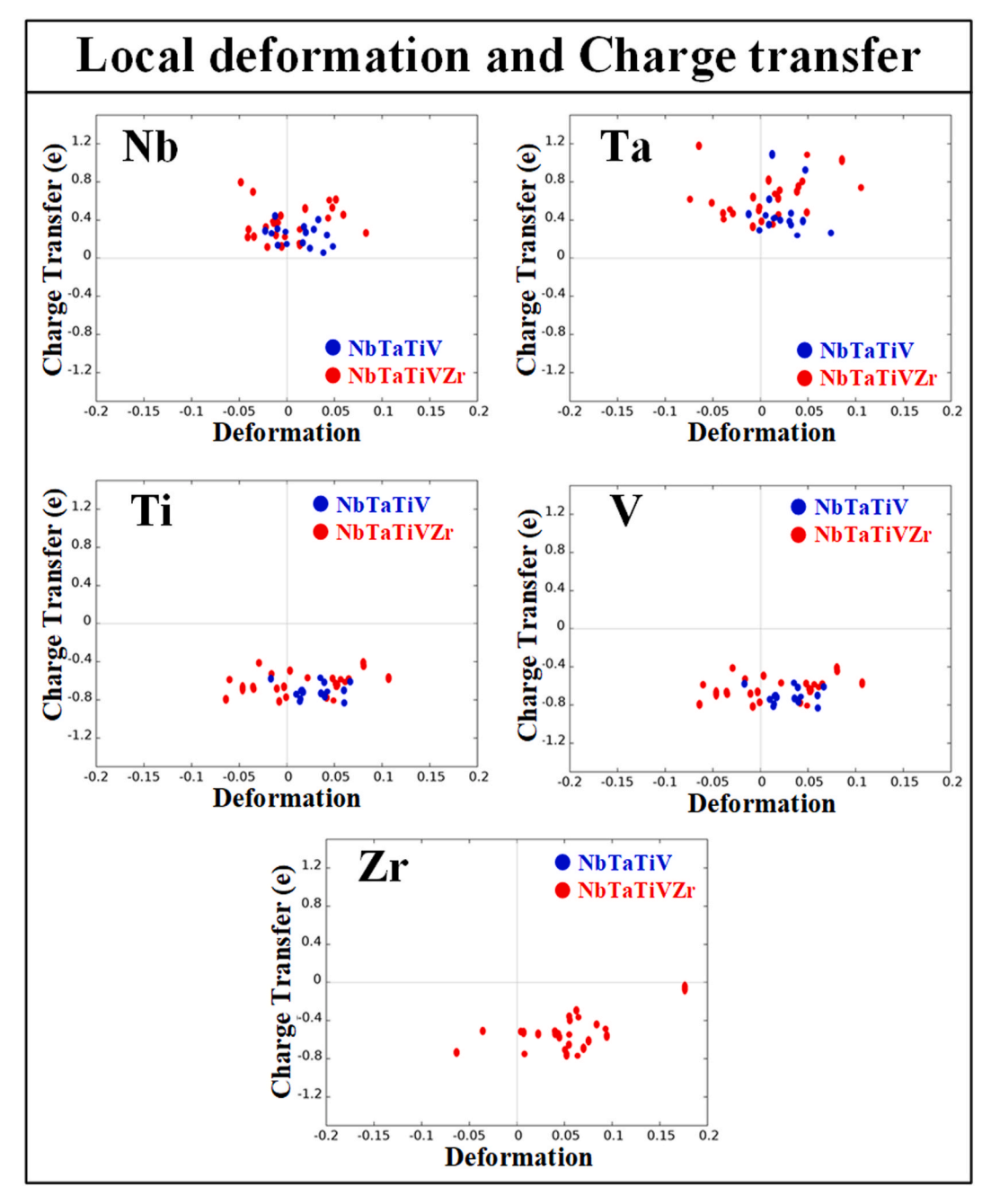


Fig. 6. Local deformation and charge transfer in NbTaTiV and NbTaTiVZr RHEAs. The charge transfer for all constituent elements in both RHEAs is separately illustrated.

BCC solid-solution phase and excellent phase stability at elevated temperatures. Hence, the dominant strengthening mechanism can be the solid-solution strengthening, which is mainly associated with severely-distorted lattices [34]. The reported works have quantitatively demonstrated the values of lattice distortions for NbTaTiV and NbTaTiVZr, indicating that the addition of the Zr element efficiently promotes distorted lattices, resulting in a higher yield strength in the alloy, as compared to the NbTaTiV HEA [34]. The measured average lattice distortions for NbTaTiV and NbTaTiVZr RHEAs are about 0.12 Å and 0.18 Å, respectively [34]. The first-principal calculation in a previous study exhibited that the variation of average nearest neighbour atomic distances in NbTaTiVZr is substantially greater than NbTaTiV, leading to a higher lattice distortion. Compared to the reported investigation on strengthening mechanisms, the present DFT calculations are in good agreement with the experimental data, showing that NbTaTiVZr has

larger distributions in both charge transfer and deformation than the NbTaTiV RHEA.

5. Conclusion

Overall, the deformation behaviors for NbTaTiV and NbTaTiVZr RHEAs have been investigated to demonstrate the unique plastic-deformation characteristics in ductile BCC RHEAs via an in-depth *insitu* neutron study. Both RHEAs have the simple solid-solution microstructures and excellent single BCC phase stability without any stress-induced phase formation/transformation during plastic deformation. The relatively-brittle NbTaTiVZr presents the typical elastic and plastic deformation behavior of the BCC-structured alloy, exhibiting elastic and plastic anisotropic feature with the significant load transfer from {110} to {200} grains during plastic deformation. However, the NbTaTiV HEA

shows elastic isotropic and reduced plastic anisotropic deformation behaviors. The unusual plastic deformation in the NbTaTiV RHEA leads to an even sharing of the applied stresses (loads) among grains with different orientations rather than the formation of stress concentration in grains with specific orientations during plastic deformation. Therefore, the homogenous load-transfer between grains with different orientations could result in excellent compressive ductility in BCC RHEAs. These observations provide a fundamental understanding of the unique deformation behavior in the ductile HEA and a road map to overcome the strength-ductility trade-off in single BCC phase RHEAs. Combining larger lattice distortion and stronger charge transfer in NbTaTiVZr qualitatively explains its higher strength and lower ductility than NbTaTiV.

Disclaimer

This report was prepared as an account of work sponsored by an agency of the United States Government. Neither the United States Government nor any agency thereof, nor any of their employees, makes any warranty, express or implied, or assumes any legal liability or responsibility for the accuracy, completeness, or usefulness of any information, apparatus, product, or process disclosed, or represents that its use would not infringe privately owned rights. Reference therein to any specific commercial product, process, or service by trade name, trademark, manufacturer, or otherwise does not necessarily constitute or imply its endorsement, recommendation, or favoring by the United States Government or any agency thereof. The views and opinions of authors expressed therein do not necessarily state or reflect those of the United States Government or any agency thereof.

CRediT authorship contribution statement

Chanho Lee: performed the scanning-electron-microscopy, Neutron diffractions, and mechanical tests, All authors contributed extensively to the work presented in this manuscript, Writing - original draft, wrote the main manuscript. All authors discussed the results and implications and commented on the manuscript at all stages. Gian Song: performed the scanning-electron-microscopy, Neutron diffractions, and mechanical tests, All authors contributed extensively to the work presented in this manuscript. Michael C. Gao: Formal analysis, designed the studied refractory high-entropy alloys and conducted the Density functional theory (DFT) analysis, All authors contributed extensively to the work presented in this manuscript. Lizhi Ouvang: Formal analysis, designed the studied refractory high-entropy alloys and conducted the Density functional theory (DFT) analysis, All authors contributed extensively to the work presented in this manuscript. Saryu J. Fensin: Writing original draft, wrote the main manuscript. All authors discussed the results and implications and commented on the manuscript at all stages, All authors contributed extensively to the work presented in this manuscript. Peter K. Liaw: Writing - original draft, wrote the main manuscript. All authors discussed the results and implications and commented on the manuscript at all stages, All authors contributed extensively to the work presented in this manuscript.

Declaration of competing interest

The authors declare that they have no known competing financial interests or personal relationships that could have appeared to influence the work reported in this paper.

Acknowledgements

The authors very much appreciate the support from the U.S. Army Office Project (W911NF-13-1-0438 and W911NF-19-2-0049) with the program managers, Drs. Michael P. Bakas, David M. Stepp, and Suveen Mathaudhu. Peter K. Liaw also thanks the support from the National

Science Foundation (DMR-1611180 and 1809640) with the program directors, Drs. Judith Yang, Gary Shiflet, and Diana Farkas. The theoretical modelling work was carried out to support the US Department of Energy's Fossil Energy Cross-Cutting Technologies Program at the National Energy Technology Laboratory (NETL). Furthermore, the present work was supported by the National Research Foundation of Korea (NRF) grant funded by the Korea government (MIST) (NO. 2019R1A4A1026125) and (No.2020R1C1C1005553). The current research used resources at the Spallation Neutron Source, a Department of Energy (DOE) Office of Science User Facility operated by the Oak Ridge National Laboratory.

This manuscript has been authored by UT-Battelle, LLC under Contract No. DE-AC05-00OR22725 with the U.S. Department of Energy. The United States Government retains and the publisher, by accepting the article for publication, acknowledges that the United States Government retains a non-exclusive, paid-up, irrevocable, worldwide license to publish or reproduce the published form of this manuscript, or allow others to do so, for United States Government purposes. The Department of Energy will provide public access to these results of federally-sponsored research in accordance with the DOE Public Access Plan (http://energy.gov/downloads/doe-public-access-plan).

References

- Y. Zhang, T.T. Zuo, Z. Tang, M.C. Gao, K.A. Dahmen, P.K. Liaw, Z.P. Lu, Microstructures and properties of high-entropy alloys, Prog. Mater. Sci. 61 (2014) 1–93.
- [2] O. Senkov, G. Wilks, D. Miracle, C. Chuang, P. Liaw, Refractory high-entropy alloys, Intermetallics 18 (9) (2010) 1758–1765.
- [3] O. Senkov, G. Wilks, J. Scott, D. Miracle, Mechanical properties of Nb 25 Mo 25 Ta 25 W 25 and V 20 Nb 20 Mo 20 Ta 20 W 20 refractory high entropy alloys, Intermetallics 19 (5) (2011) 698–706.
- [4] O. Senkov, J. Scott, S. Senkova, F. Meisenkothen, D. Miracle, C. Woodward, Microstructure and elevated temperature properties of a refractory TaNbHfZrTi alloy, JMatS 47 (9) (2012) 4062–4074.
- [5] O. Senkov, J. Scott, S. Senkova, D. Miracle, C. Woodward, Microstructure and room temperature properties of a high-entropy TaNbHfZrTi alloy, J. Alloys Compd. 509 (20) (2011) 6043–6048.
- [6] O. Senkov, S. Senkova, C. Woodward, Effect of aluminum on the microstructure and properties of two refractory high-entropy alloys, Acta Mater. 68 (2014)
- [7] Y. Zou, S. Maiti, W. Steurer, R. Spolenak, Size-dependent plasticity in an Nb 25 Mo 25 Ta 25 W 25 refractory high-entropy alloy, Acta Mater. 65 (2014) 85–97.
- [8] Y. Zou, H. Ma, R. Spolenak, Ultrastrong ductile and stable high-entropy alloys at small scales, Nat. Commun. 6 (2015) 7748.
- [9] C.-C. Juan, M.-H. Tsai, C.-W. Tsai, C.-M. Lin, W.-R. Wang, C.-C. Yang, S.-K. Chen, S.-J. Lin, J.-W. Yeh, Enhanced mechanical properties of HfMoTaTiZr and HfMoNbTaTiZr refractory high-entropy alloys, Intermetallics 62 (2015) 76–83.
- [10] N. Guo, L. Wang, L. Luo, X. Li, Y. Su, J. Guo, H. Fu, Microstructure and mechanical properties of refractory MoNbHfZrTi high-entropy alloy, Mater. Des. 81 (2015) 87–94.
- [11] O. Senkov, C. Woodward, Microstructure and properties of a refractory NbCrMo0. 5Ta0. 5TiZr alloy, Mater. Sci. Eng., A 529 (2011) 311–320.
- [12] O. Senkov, C. Woodward, D. Miracle, Microstructure and properties of aluminumcontaining refractory high-entropy alloys, JOM 66 (10) (2014) 2030–2042.
- [13] H.L. Huang, Y. Wu, J.Y. He, H. Wang, X.J. Liu, K. An, W. Wu, Z.P. Lu, Phase-transformation ductilization of brittle high-entropy alloys via metastability engineering, Adv. Mater. 29 (30) (2017) 7.
- [14] Z. Li, K.G. Pradeep, Y. Deng, D. Raabe, C.C. Tasan, Metastable high-entropy dualphase alloys overcome the strength-ductility trade-off, Nature 534 (7606) (2016) 227–231.
- [15] S. Gorsse, M. Nguyen, O.N. Senkov, D.B. Miracle, Database on the mechanical properties of high entropy alloys and complex concentrated alloys, Data in Brief 21 (2018) 2664–2678.
- [16] J.-P. Couzinié, O. Senkov, D. Miracle, G. Dirras, Comprehensive data compilation on the mechanical properties of refractory high-entropy alloys, Data in brief 21 (2018) 1622–1641.
- [17] E. Mak, B. Yin, W. Curtin, A ductility criterion for bcc high entropy alloys, J. Mech. Phys. Solid. 152 (2021) 104389.
- [18] Y.-J. Hu, A. Sundar, S. Ogata, L. Qi, Screening of generalized stacking fault energies, surface energies and intrinsic ductile potency of refractory multicomponent alloys, Acta Mater. 210 (2021) 116800.
- [19] C. Lee, Y. Chou, G. Kim, M.C. Gao, K. An, J. Brechtl, C. Zhang, W. Chen, J. D. Poplawsky, G. Song, R. Yang, C. Yi-Chia, K.L. Peter, Lattice-distortion-enhanced yield strength in a refractory high-entropy alloy, Adv. Mater. 32 (49) (2020) 2004029.
- [20] C. Lee, G. Song, M.C. Gao, R. Feng, P. Chen, J. Brechtl, Y. Chen, K. An, W. Guo, J. D. Poplawsky, S. Li, A.T. Samaei, W. Chen, A. Hu, H. Choo, P.K. Liaw, Lattice

- distortion in a strong and ductile refractory high-entropy alloy, Acta Mater. 160 (2018) 158–172.
- [21] K. An, H.D. Skorpenske, A.D. Stoica, D. Ma, X.-L. Wang, E. Cakmak, First in situ lattice strains measurements under load at VULCAN, MMTA 42 (1) (2011) 95–99.
- [22] X.-L. Wang, T. Holden, G.Q. Rennich, A. Stoica, P.K. Liaw, H. Choo, C.R. Hubbard, VULCAN—the engineering diffractometer at the SNS, Phys. B Condens. Matter 385 (2006) 673–675.
- [23] K. An, VDRIVE-data Reduction and Interactive Visualization Software for Event Mode Neutron Diffraction, ORNL Report No. ORNL-TM-2012-621, Oak Ridge National Laboratory, Oak Ridge, TN, 2012.
- [24] G. Kresse, J. Hafner, Ab initio molecular dynamics for liquid metals, Phys. Rev. B 47 (1993) 558–561.
- [25] G. Kresse, J. Furthmüller, Efficient iterative schemes for ab initio total-energy calculations using a plane-wave basis set, Phys. Rev. B 54 (1996) 11169–11186.
- [26] A. Zunger, S.H. Wei, L.G. Ferreira, J.E. Bernard, Special quasirandom structures, Phys. Rev. Lett. 65 (3) (1990).
- [27] A. van de Walle, M. Asta, G. Ceder, The alloy theoretic automated Toolkit: a user guide, Calphad 26 (4) (2002) 539–553.
- [28] A. van de Walle, Multicomponent multisublattice alloys, nonconfigurational entropy and other additions to the Alloy Theoretic Automated Toolkit, Calphad 33 (2) (2009) 266–278.
- [29] M.C. Gao, C. Niu, C. Jiang, D.L. Irving, Chapter 10: applications of special quasirandom structures to high-entropy alloys, in: M.C. Gao, J.W. Yeh, P.K. Liaw, Y. Zhang (Eds.), High-Entropy Alloys: Fundamentals and Applications, Springer, Cham, Switzerland, 2015.
- [30] P.E. Blochl, Projector augmented-wave method, Phys. Rev. B 50 (24) (1994)

- [31] J.P. Perdew, K. Burke, M. Ernzerhof, Generalized gradient approximation made simple, Phys. Rev. Lett. 77 (1996) 3865–3868.
- [32] H.J. Monkhorst, J.D. Pack, Special points for brillouin-zone integrations, Phys. Rev. B 13 (12) (1976) 5188.
- [33] M. Methfessel, A.T. Paxton, Phys. Rev. B 40 (6) (1989) 3616.
- [34] C. Lee, Y. Chou, G. Kim, M.C. Gao, K. An, J. Brechtl, C. Zhang, W. Chen, J. D. Poplawsky, G. Song, Y. Ren, Y.-C. Chou, P.K. Liaw, Lattice-distortion-enhanced yield strength in a refractory high-entropy alloy, Adv. Mater. 32 (49) (2020) 2004029.
- [35] S. Huang, D.W. Brown, B. Clausen, Z. Teng, Y. Gao, P.K. Liaw, In situ neutrondiffraction studies on the creep behavior of a ferritic superalloy, MMTA 43 (5) (2012) 1497–1508.
- [36] G.M. Stoica, A.D. Stoica, M.K. Miller, D. Ma, Temperature-dependent elastic anisotropy and mesoscale deformation in a nanostructured ferritic alloy, Nat. Commun. 5 (1) (2014) 1–8.
- [37] Y. Wu, W. Liu, X. Wang, D. Ma, A.D. Stoica, T. Nieh, Z. He, Z. Lu, In-situ neutron diffraction study of deformation behavior of a multi-component high-entropy alloy, Appl. Phys. Lett. 104 (5) (2014), 051910.
- [38] M. Daymond, H. Priesmeyer, Elastoplastic deformation of ferritic steel and cementite studied by neutron diffraction and self-consistent modelling, Acta Mater. 50 (6) (2002) 1613–1626.
- [39] Y. Tomota, P. Lukas, S. Harjo, J. Park, N. Tsuchida, D. Neov, In situ neutron diffraction study of IF and ultra low carbon steels upon tensile deformation, Acta Mater. 51 (3) (2003) 819–830.
- [40] W. Tang, E. Sanville, G. Henkelman, A grid-based Bader analysis algorithm without lattice bias, J. Phys. Condens. Matter 21 (8) (2009), 084204.